Int. J. Therm. Sci. (2001) 40, 981–997

S1290-0729(01)01284-4/FLA

Numerical experiments in the simulation of enhanced oil recovery from a porous formation

Tanuja Sheorey, Krishnamurthy Muralidhar*, Partha Pratim Mukherjee

Department of Mechanical Engineering, Indian Institute of Technology Kanpur, Kanpur 208 016 UP, India

(Received 4 July 2000, accepted 30 January 2001)

Abstract — A numerical reservoir simulation model for the study of enhanced oil recovery (EOR) from a porous formation has been presented. The resistance to oil movement arises from viscous forces in the fluid phase as well as surface tension. Viscous forces can be lowered by hot water injection into the formation or by raising the formation temperature. These methods have been numerically analyzed in the present study. The role of the operating parameters such as the injection pressure and temperature on oil recovery has been reported. Displacement of oil by water is clearly brought out by the saturation and the temperature profiles.

The numerical solution of the EOR problem experiences growth of errors during long time integration, particularly on large regions. Possible reasons are scatter in the constitutive relationship data, inexact outflow boundary condition and round-off errors in the calculation of the matrix inverse. The nature of these errors has been addressed in the present work. To solve the computationally intensive field-scale problems, two domain decomposition algorithms namely, Schwarz's and Uzawa's algorithms have been evaluated.

Results show that oil recovery can be improved when the formation temperature is higher, or the injection temperature and pressure are raised. Adverse results can however be obtained when the injection temperature exceeds a critical value. Optimum conditions prevail when the speed of the oil–water interface is matched with that of the thermal front. As a computational tool, the domain decomposition algorithms are conditionally seen to improve the numerical performance of the oil recovery codes. © 2001 Éditions scientifiques et médicales Elsevier SAS

oil recovery / porous medium / oil–water flow / flow in porous media / temperatures in porous media / numerical solution

Nomenclature

Bi	Biot number, $= h\,\mathrm{Y}/k_h$	
c	specific heat capacity	$\mathrm{J{\cdot}kg^{-1}{\cdot}K^{-1}}$
h	heat transfer coefficient between the porous formation and its environment	$\mathrm{W{\cdot}m^{-2}{\cdot}K^{-1}}$
K	absolute permeability of the formation	$\mathrm{m^2}$
k_{ri}	relative permeability of the ith phase	
k_h	thermal conductivity of the porous medium	$\mathrm{W{\cdot}m^{-1}{\cdot}K^{-1}}$
L	Laplacian operator $= \nabla^2$	
n, m	grid points along the x and y axes	
$p_{c_{ow}}$	capillary pressure between oil and water phases	$\mathrm{N{\cdot}m^{-2}}$
p_i	phase pressure of the ith phase . . .	$\mathrm{N{\cdot}m^{-2}}$
PPV	percentage pore volume of oil recovery (equation (9))	
S_i	saturation of the ith phase in the porous region	
$t, \Delta t$	time and time step	s
T	temperature	°C
T_f	temperature of rock formation . .	°C
u, v	Darcy velocity	$\mathrm{m{\cdot}s^{-1}}$
x, y	Cartesian coordinates	m
$\Delta x, \Delta y$	grid size along x and y axes	
X, Y	domain dimension in x and y directions respectively	

Greek symbols

α	interface convergence parameter in Uzawa's algorithm	
β_i	expansivity of the ith phase . . .	$\mathrm{°C^{-1}}$
ε	porosity	
Γ	interface boundary between the subdomains	
μ_i	dynamic viscosity of the ith phase	$\mathrm{N{\cdot}m{\cdot}s^{-1}}$
λ_i	mass flux of the ith phase $= -k_{ri}\,\partial p_i/\partial x$	
ρ_i	density of the ith phase	$\mathrm{kg{\cdot}m^{-3}}$

* Correspondence and reprints.
E-mail address: kmurli@iitk.ac.in (K. Muralidhar).

θ	interface convergence parameter in Schwarz's algorithm	
$\Omega, \partial\Omega$	physical domain and its boundary	
ξ_i	compressibility of the ith phase .	Pa^{-1}

Superscript

k	current time step

Subscript

f	formation
i	index representing oil or water
inj	injection
o	oil
ref	reference
R	solid phase of the porous formation
w	water

1. INTRODUCTION

The technology of enhanced oil recovery (EOR) from porous formations has been described by various authors [1, 2]. EOR is generally applicable to the secondary or the tertiary phase of recovery in the productive life of the reservoir. The primary recovery is by a natural drive mechanism owing to the pressure of the resident fluid in the formation. The secondary recovery refers to techniques whose purpose is to maintain the reservoir pressure, by water injection for example. Here, the injected fluid displaces the resident fluid across a moving interface. The speed of the interface is controlled by a combination of various physico–chemical processes. The heavier, low specific gravity oils are too viscous to move to the production wells by this technique at rates sufficient to justify an economical operation. Thermal methods are therefore used at the tertiary phase to recover hydrocarbons by introducing heat to lower the oil viscosity. Hot water injection and *in situ* combustion are examples of such thermal methods.

Enhanced oil recovery has all the characteristics of multiphase flow in a porous medium. The flow behavior is dictated by gravitational, viscous and capillary forces. The gravity force causes phase migration in the direction of the gravitational field [3]. The viscous and capillary forces influence the relative phase movement. Moreover, the capillary forces play a fundamental role in controlling the phase distribution in heterogenous porous media [4]. Mathematical modelling is a useful tool for delineating the important flow mechanisms in a reservoir and thus predict its overall performance [4–8].

The primary unknowns in oil–water flow through a porous region are the individual pressures of the fluid phases, water saturation and the locally averaged temperature. The governing equations for the oil and water pressures have been solved numerically using a central difference scheme. In the present work a fully implicit pressure-based formulation has been used. The energy equation has been solved using an operator-splitting algorithm [9]. The saturation profiles have been obtained through the appropriate constitutive relations. The formulation adopted in the present work carries over from [9]. Numerical results have been reported for large length and time scales and over a wide range of parameters. The growth and control of numerical errors during time integration have been addressed. Further, the possibility of applying domain decomposition techniques for the simulation of oil recovery has been discussed in the present work.

2. MATHEMATICAL FORMULATION

The two-dimensional physical domain that is considered for analysis is a thin porous layer shown in *figure 1*. The domain is filled with oil at a prescribed initial saturation of 0.8, the rest being water. The temperature and pressure of the oil–rich formation are also initially prescribed. The medium is taken to be bounded by impermeable and thermally non-conducting rocks at $y = 0$ and $y = \mathrm{Y}$. Water is injected at a pressure higher than that of the formation at $x = 0$. A mixture of oil and water is recovered at $x = \mathrm{X}$. The mathematical formulation of the conservation equations are summarized below [4–7]:

Conservation of mass. The mass balance equation for each of the phases is given by:

$$\frac{\partial}{\partial t}(\varepsilon S_i \rho_i) + \nabla \cdot (\rho_i u_i) = 0 \quad i = \text{oil, water} \qquad (1)$$

Momentum. The phase momentum equations in the form of the generalized Darcy's law for each phase, namely oil and water are written as:

$$u_i = -\frac{K k_{\mathrm{r}i}}{\mu_i} \nabla p_i \qquad (2)$$

Here, the gravity over-ride term has been neglected since the formation has been assumed to be thin and the vertical temperature gradient is negligible. Equations (1) and (2) governing transient two-phase flow through a homogeneous, isotropic porous medium can be combined in terms of the phase pressures to yield:

$$-S_o\beta_o\frac{\partial T}{\partial t}+S_o\xi_o\frac{\partial p_w}{\partial t}-\frac{dS_w}{dp_{c_{o,w}}}\left[\frac{\partial p_o}{\partial t}-\frac{\partial p_w}{\partial t}\right]=\frac{1}{\rho_o}\nabla.\left[\frac{Kk_{ro}\rho_o}{\mu_o\varepsilon}\right]\nabla p_o \quad (3)$$

$$-S_w\beta_w\frac{\partial T}{\partial t}+S_w\xi_w\frac{\partial p_w}{\partial t}-\frac{dS_w}{dp_{c_{o,w}}}\left[\frac{\partial p_o}{\partial t}-\frac{\partial p_w}{\partial t}\right]=\frac{1}{\rho_w}\nabla.\left[\frac{Kk_{rw}\rho_w}{\mu_w\varepsilon}\right]\nabla p_w \quad (4)$$

Conservation of energy. Assuming local thermal equilibrium among contiguous phases, the equation for conservation of energy in two-phase flow can be expressed as:

$$\frac{\partial T}{\partial t}+U\frac{\partial T}{\partial x}+V\frac{\partial T}{\partial y}=\frac{k_h}{\sigma_T}\nabla^2 T \quad (5)$$

where

$$U=\frac{u_o(\rho c)_o+u_w(\rho c)_w}{\sigma_T}$$

$$V=\frac{v_o(\rho c)_o+v_w(\rho c)_w}{\sigma_T}$$

$$\sigma_T=\varepsilon\left[(1-S_w)(\rho c)_o+S_w(\rho c)_w\right]+(1-\varepsilon)(\rho c)_R \quad (6)$$

and T is the local volume averaged temperature.

Equations (3) and (4) for oil and water pressure and equation (5) for temperature form a closed system of equations. The above equations have been solved simultaneously for oil and water pressures and the average temperature. These equations have to be supplemented by constitutive relations of the form:

$$k_{rw}=k_{rw}(S_w)$$

$$k_{ro}=k_{ro}(S_w)$$

$$p_o-p_w=p_{c_{ow}}(S_w)$$

$$S_o+S_w=1$$

$$\frac{\rho_i}{\rho_{i,ref}}=1+\xi_i(p_i-p_{i,ref})-\beta_i(T-T_{ref}) \quad i=o,w \quad (7)$$

Detailed form of these relationships along with the properties of the reservoir fluids are given in Appendix A.

Unique solutions for the flow and the thermal field are obtained by supplying suitable initial and boundary conditions. These correspond to a specified initial water pressure, saturation and temperature in the physical domain. Water pressure, saturation and temperature are specified on the inflow and the outflow planes for all time. The bounding surfaces at $y = 0$ and y = Y have been taken to be impervious to flow and thermally nonconducting. These conditions are summarized as:

$$t=0:\ S_w,\ p_w,\ T \quad \text{prescribed, all } x \text{ and } y$$

$$x=0,\text{X}:\ S_w,\ p_w,\ T \quad \text{prescribed, all } t$$

$$y=0,\text{Y}:\ \frac{\partial}{\partial y}(p_o,\ p_w)=0$$

$$\frac{\partial T}{\partial y}+Bi(T-T_f)=0, \quad \text{all } t \quad (8)$$

The Biot number represents the extent of heat loss to the side walls. For an insulating wall, $Bi = 0$. Typical values of the prescribed pressures and temperatures employed in the simulation are shown in *figure 1*.

One of the important measures of oil recovery is the percentage pore volume (PPV) defined as

$$\text{PPV}=\frac{\text{Initial volume of oil}-\text{Present volume of oil}}{\text{Pore volume}}\times 100 \quad (9)$$

The increase in PPV with time has been reported in the present study for various injection conditions.

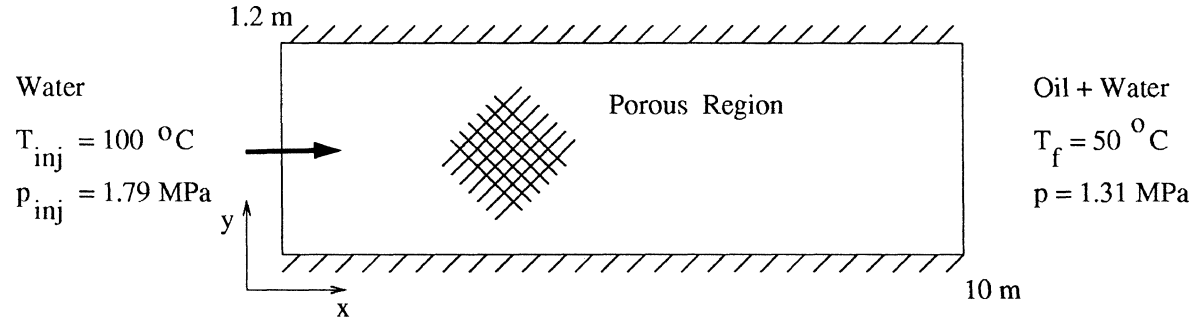

Figure 1. Schematic drawing of the physical region and the coordinate system.

3. NUMERICAL SOLUTION

The oil and water pressure equations and temperature equation have been discretized using a finite difference scheme. Spatial derivatives are evaluated using central differencing. Time derivatives are discretized using the forward difference formula. The scheme is fully implicit in time. However, the derivatives of temperature appearing in equations (3) and (4) have been evaluated at the earlier time level. The solution technique is iterative and involves the linearization of the non-linear product terms for the evaluation of the finite difference coefficients [9].

For a $n \times m$ grid in the physical domain, the discretized equations contain $2 \times n \times m$ unknowns to be solved simultaneously for the oil and water pressures. A sparse matrix solver based on Gaussian elimination [10] has been used to invert the matrix.

The energy equation has been solved by the operator splitting algorithm [9]. In this method, the energy equation

$$\frac{\partial T}{\partial t} + U\,\frac{\partial T}{\partial x} + V\,\frac{\partial T}{\partial y} = \left(\frac{k_{\mathrm{h}}}{\sigma_T}\right)\nabla^2 T \qquad (10)$$

is split into the following steps:

$$\text{Predictor:} \quad \frac{\partial T}{\partial t} + U\,\frac{\partial T}{\partial x} + V\,\frac{\partial T}{\partial y} = 0 \quad \text{over } \Delta t \qquad (11)$$

$$\text{Corrector:} \quad \frac{\partial T}{\partial t} = \left(\frac{k_{\mathrm{h}}}{\sigma_T}\right)\nabla^2 T \quad \text{over } \Delta t \qquad (12)$$

The predictor step is solved by the method of characteristics as:

$$T_{\mathrm{P}}^{n+1}\big(U'(t+\Delta t) - \xi\big) = T_{\mathrm{Q}}^{n}\big(U't - (\xi - \Delta\xi)\big) \qquad (13)$$

where, $\Delta\xi = U'^{n}\Delta t$, U' is the resultant local velocity, and ξ is the local streamline direction passing through points P and Q. Here point P stands for the node (i, j) of the grid. The temperature T_{Q} is obtained through interpolation over the temperature field at the previous time instant.

The corrector step consists of solving the two-dimensional unsteady state heat conduction equation. The Alternating Direction Implicit (ADI) technique has been used for this purpose. The solution obtained from the predictor step is the initial condition for the ADI calculation.

The system of equations governing the distribution of oil and water pressures and temperature are non-linear and strongly coupled. A simultaneous solution approach has been adopted to retain the coupling between the phase pressures. The coupling between the phase pressures and tempertaure has been resolved by iteration.

A convergence criterion of 0.1% between successive iterations at each time level has been used in the present study. For a region size of 10 m $\times$ 1.2 m, a grid consisting of 101 $\times$ 11 nodes for each of the variables p_{o}, p_{w} and T has been used. For larger domains, the number of nodes was proportionally increased. This level of refinement has been found to be adequate to obtain a grid-independent solution. The time step for all the calculations was kept at 0.01 hour. The correctness of the computer code has been tested by solving linear and non-linear transient heat conduction equations. The matrix obtained from the pressure equations has been solved by both the sparse matrix solver based on Gaussian elimination as well as the preconditioned conjugate gradient method. The two sets of results were seen to match very well. The predictions of the computer code developed in the present work also matched with the test cases of [7], particularly the difficult water bank simulation.

3.1. Domain decomposition technique

EOR applications invariably require intensive computations because of the large size of the physical domains and their complex geometries. With the availability of parallel computers, there exists a great potential for reducing the CPU time as well as memory. However parallel computers require suitable algorithms to make use of the distributed nature of the processor architecture. In this connection, two domain decomposition algorithms have been tested in the present study to examine their suitability for numerical calculations of oil recovery.

The basic approach of domain decomposition is that a large region is divided into many subdomains that are linked at overlapping regions or along interfaces [11–15]. Overlapping regions have a disadvantage since the rate of convergence deteriorates as the extent of overlap is reduced [15]. The present discussion is restricted to non-overlapping subdomains. The governing equations are solved independently in each subdomain with assumed interface conditions of the dependent variables and their fluxes. The interface treatment adopted in the present study are based on the Schwarz's technique [15] and Uzawa's algorithm [12]. Both algorithms are iterative since the variables and the fluxes at the interface are assumed. A close tolerance is required for convergence to maintain accuracy over the entire physical domain, particularly when long time periods are involved.

Schwarz's technique is first discussed. The 2-domain non-overlapping Schwarz's method can be stated as follows [15]. Let the original problem be posed in terms of a generic variable u as:

$$Lu^{k+1} = f \quad \text{on } \Omega = \Sigma\Omega_i,\ i = 1, 2$$

with suitable boundary conditions. The equivalent problem in the subdomains can be written as:

$$Lu_i^{k+1} = f \quad \text{on } \Omega_i$$

with the interface conditions:

subdomain 1:

$$\text{(implicit)} \quad \Phi\left(u_1^{k+1}\right) = \theta\left(u_2^{k+1}\right) + (1-\theta)\Phi\left(u_1^{k+1}\right) \quad \text{on } \Gamma \tag{14}$$

subdomain 2:

$$\text{(implicit)} \quad \Psi\left(u_2^{k+1}\right) = \Psi\left(u_1^{k+1}\right) \quad \text{on } \Gamma \tag{15}$$

where θ is a suitable relaxation parameter, Φ represents the essential Dirichlet condition and Ψ is a Neumann condition.

The Schwarz's technique can be seen as a method of applying the continuity conditions in the variable and its normal derivative at the interface between the two subdomains [11]. The problems in the subdomains are coupled and can only be iteratively solved.

In Uzawa's algorithm, each problem in the subdomains is subjected to an assumed flux boundary condition at the interface and later solved by an implicit numerical scheme [12]. For a globally converged solution the dependent variables and their normal derivatives are required to be continuous on the interface of the subdomains. Hence, the assumed fluxes are updated as:

$$\lambda_i^2 = \lambda_i^1 + \alpha\left(u_2^1|_\Gamma - u_1^1|_\Gamma\right)$$

where α is the interface convergence parameter and

$$\lambda = k(u)\,\frac{\partial u}{\partial x}$$

is the interfacial flux. The two domain decomposition algorithms referred above due to their inherent parallelism can be coded on a parallel computer.

4. RESULTS AND DISCUSSION

Results obtained from the numerical simulation of enhanced oil recovery from a porous formation are discussed in the present section. The amount of oil displaced from the formation depends on a variety of factors, including the formation pressure and temperature, and the injection pressure and temperature. Other quantities such as oil viscosity and its dependence on temperature, porosity and permeability of the formation also play an important role. These are however fixed for a given site being analyzed. In view of the nonlinear constitutive relationships, it can be anticipated that the influence of the controlling parameters such as pressure and temperature will not be uniform. To explore this aspect, a detailed parametric study of the effect of the formation and injection properties on oil recovery has been carried out in the present work.

An unexpected observation that was noticed during simulation was the appearance of oscillations in the numerical solution. The oscillations appeared initially in the saturation profiles that later affected the pressure and temperature profiles as well. It is proposed here that the numerical oscillations are related to the accumulation of the discretization errors during time marching. This is to be anticipated in problems that do not have a well-defined steady state, stationary or dynamic. The errors were seen to originate from the outflow plane, possibly due to reflections from a Dirichlet boundary condition. This observation shows that the oil–water migration in the porous medium is a flow problem, despite the diffusion-like appearance of the governing equations.

The saturation profile being the first to be affected by discretization errors can be explained as follows. Water saturation is a function of the capillary pressure $(p_o - p_w)$, which is of the order of a few kilopascals (kPa). The individual pressures are themselves of the order of a few megapascals (MPa). Thus, small errors in the water and oil pressures (despite the use of a stringent convergence criterion between successive iterations) can appear as a larger error in the capillary pressure and thus in water saturation. Strategies for reducing the influence of the oscillations and increasing the range of numerical integration in the time direction have been discussed in Section 4.2.

The third aspect of the present work comprises of assessing the suitability of the domain decomposition technique for EOR applications. The performance of Schwarz's technique and Uzawa's algorithm in the context of EOR has been reported in the present study. The algorithms have been applied to two and four subdomains. In principle, they can be extended to any number of subdomains.

Numerical results of EOR have been presented under the following heads.

(1) Parametric study of the reservoir performance,
(2) Treatment of numerical oscillations,
(3) Domain decomposition.

4.1. Parametric study of the reservoir performance

A porous formation of size 10 m × 1.2 m has been taken up for evaluation. The reservoir performance has been studied with respect to the temperature of the formation, the injection pressure and temperature of water and their effect on the oil recovery, namely PPV (equation (9)). The results are presented in two parts: (a) isothermal injection where the injected water has the same temperature as the formation and (b) non-isothermal injection, where the injected water is at a higher temperature.

Isothermal injection

Effect of formation temperature. Four different formation temperatures (T_f) 30 °C, 40 °C, 50 °C and 60 °C have been taken up for the study. Generally, the formation temperature is an intrinsic property of the formation and is site-specific. Recent technologies such as *in-situ* combustion however show the possibility of raising the formation temperature to a desired higher value. In the simulation, the injection and formation pressures are maintained at 1.79 MPa and 1.31 MPa, respectively. These pressures are to be interpreted as those of water. The corresponding pressures for oil are computed by fixing the water saturation at the inflow and outflow planes and using the constitutive relationship of capillary pressure with respect to water saturation. The evolution of the saturation profiles with time at a formation temperature of 50 °C is seen in *figure 2(a)*. Overall, there is rise in water saturation with time, indicating a steady oil displacement process. *Figure 2(b)* shows the effect of T_f on the water saturation profile at the end of 5 hours of injection. The effect of an increase in the formation temperature is to lower oil viscosity and hence the viscous resistance to fluid motion. Thus an increase in oil recovery with the formation temperature is to be anticipated. *Figure 2(b)* shows this to be true, on an average, since the curve for $T_f = 40$ °C lies above the one for 30 °C, but below 50 °C. Locally there are regions where the saturation falls to a lower value, and is later followed by an increase. This is to be interpreted as the accumulation of oil just beyond the water pool where the water saturation shows an increase above its neighbourhood values. At 50 °C, there is a uniform increase in water saturation at all the x-locations. This increase is more pronounced at 60 °C owing to a sharp fall in oil viscosity.

Effect of injection pressure. With injection pressure of water increasing, the difference with respect to the pressure of the resident fluids increases, thereby increasing PPV. The water pressure profiles at the end of 5 hours for various injection pressures are compared in *figure 3(a)*. The oil pressures are quite close to the water pressures everywhere and have not been separately shown. The average slope of the pressure profile is proportional to the flow rate in the porous medium. A reduction in the flow rate with increasing time is obtained,

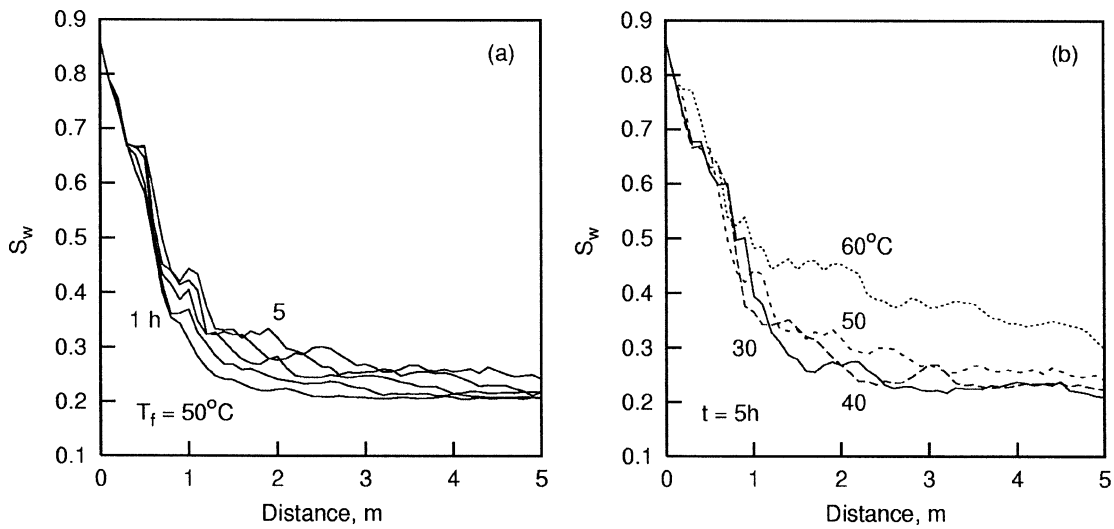

Figure 2. Isothermal injection: (a) Evolution of saturation profile at $T_f = 50$ °C; (b) Effect of the formation temperature on water saturation.

a result common to diffusion-dominated problems. *Figure 3(a)* shows an increasing slope with injection pressure, confirming an increase in oil recovery. The pressure profiles (pressures being the basic unknowns of the numerical algorithm) are themselves individually smooth. The saturation profiles for the condition referred above are shown in *figure 3(b)*. The saturation profiles reveal some scatter, being dependent on the oil-to-water pressure difference and an experimentally determined constitutive relationship.

Oil recovery. The effect of the formation temperature on oil recovery is shown in *figure 4(a)*. The increase in PPV at 50 and 60 °C is along the expected lines.

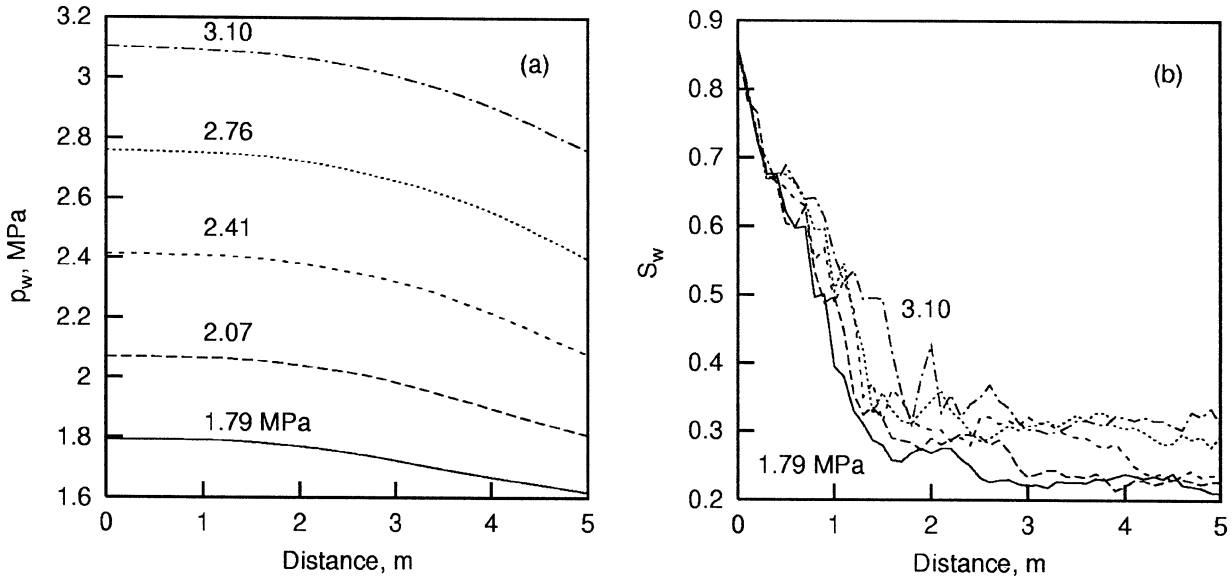

Figure 3. Isothermal injection: Effect of the injection pressure on: (a) The water pressure profile ($t = 5$ h); (b) The saturation front ($t = 5$ h).

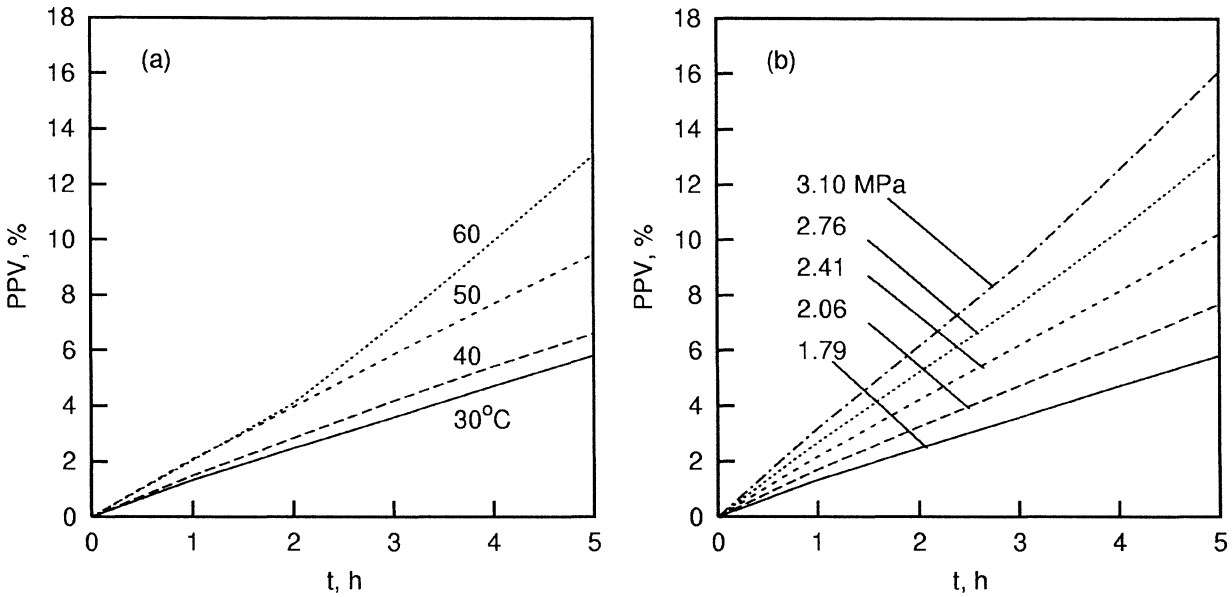

Figure 4. Increase in oil recovery with time during isothermal injection: Effect of: (a) Formation temperature; (b) Injection pressure.

With the increase in T_f, viscous resistance to flow reduces resulting in a greater oil displacement. This increase is however non-uniform, being disproportionately higher at higher temperatures. The increase cannot be sustained indefinitely, owing to the accumulation of oil beyond the water front. This topic is discussed in the next section.

Figure 4(b) shows the effect of the injection pressure on oil recovery at $T_f = 30\,^{\circ}C$. The increase of PPV is from 5.8% at 1.79 MPa to 16% at 3.10 MPa at the end of 5 hours of real time. The saturation front at other injection pressures studied are also evolving to essentially the same form as in *figure 2(a)* at an injection pressure of 1.79 MPa, all being diffusion-dominated. Thus over the range of parameters studied, the saturation front is seen to have a better stability with respect to pressure as compared to the temperature of the porous region. One can then conclude that raising the injection pressure would give a predictable increase in oil recovery as against raising the formation temperature.

Non-isothermal injection

Effect of formation temperature. Results have been obtained for four different formation temperatures in the range 30 °C through 60 °C. The injection pressure has been maintained at its nominal value of 1.79 MPa and the formation pressure is 1.31 MPa. Water is injected at a temperature of 100 °C. *Figure 5(a)* compares the temperature profiles at the end of 5 hours of injection for various values of the formation temperature. *Figure 5(a)* indicates a front-like movement of the temperature field, driven primarily by a lowered viscous resistance of the oil–water system. With increasing formation temperature, the speed of the temperature front also increases. Since oil viscosity reduces very sharply with temperature, a very high front speed is realized at $T_f = 60\,^{\circ}C$. The corresponding water saturation plot namely, a comparison at the end of 5 hours are shown in *figure 5(b)*. Saturation fronts are clearly visible in the figure. *Figure 5* establishes a close association between the saturation and the temperature fronts and confirms that the mobility of oil is linked to the lowering of its viscosity. The great increase in the speed of the thermal front at 60° is reproduced in terms of saturation as well in *figure 5(b)*. A new observation can be made from the water saturation profiles for formation temperatures upto 50 °C (*figure 5(b)*). With the passage of time, these profiles show a dip just ahead of the front position below the initial formation value. This indicates an accumulation of oil that has been mobilized by the thermal front. The viscous resistance beyond the thermal front is determined by the formation temperature. Hence the mobility of oil is restricted to the region ahead of the thermal front. As a consequence, oil recovery is adversely affected since the displaced oil does not reach the outflow plane. At 60 °C, the viscous resistance beyond the front, throughout the formation is reduced and oil does not accumulate within the physical domain.

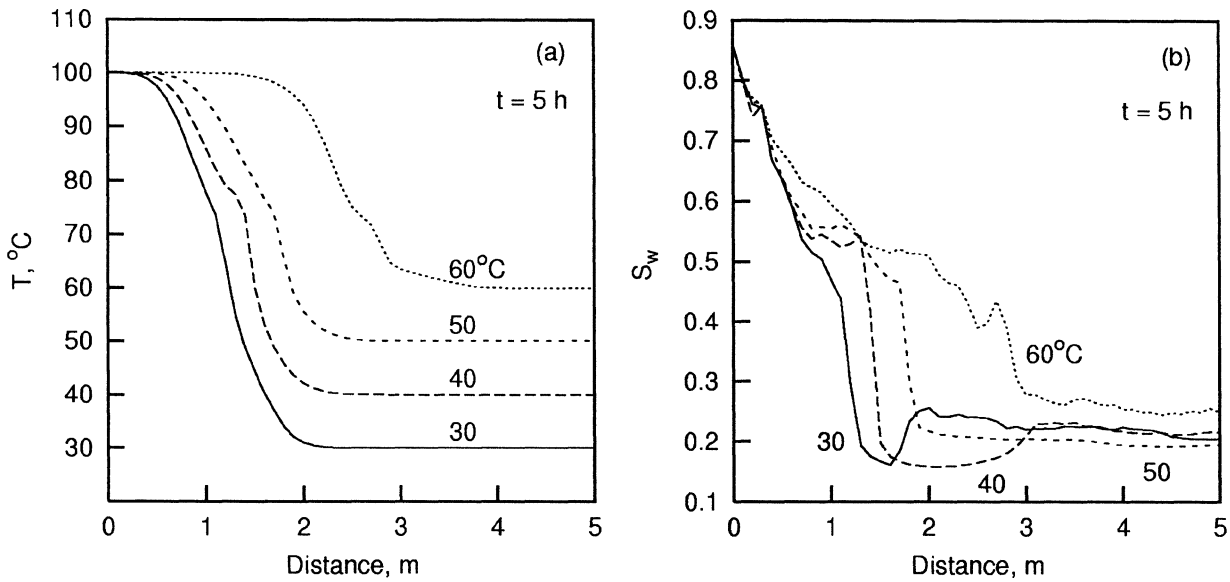

Figure 5. Non-isothermal injection: Effect of the formation temperature on the: (a) Temperature profile; (b) Saturation profile.

Effect of injection temperature. Results have been presented below for injection temperatures in the range 100–200 °C. The formation temperature in the calculations is 50 °C, while the injection and the formation pressures are 1.79 and 1.31 MPa, respectively. Temperature profiles in the formation at the end of 5 hours are shown in *figure 6(a)*, for various injection temperatures. All profiles are seen to be front-dominated. The corresponding saturation plot is shown in *figure 6(b)*. Some of the results presented in *figure 5* carry over to the present discussion. Primarily, the accumulation of oil just beyond the thermal/saturation front leading to water saturation falling below the initial formation value is reproduced here at all injection temperatures. The magnitude of the problem is aggravated at higher injection temperatures. A closely related phenomenon is the appearance of a kink in the saturation curve, which gradually levels off with increasing time. This result can be explained as follows. In non-isothermal injection, the thermal front moves through the formation at a rate different from the injected fluid, the latter being determined by the injection pressure. When the thermal front moves faster, it lowers oil viscosity

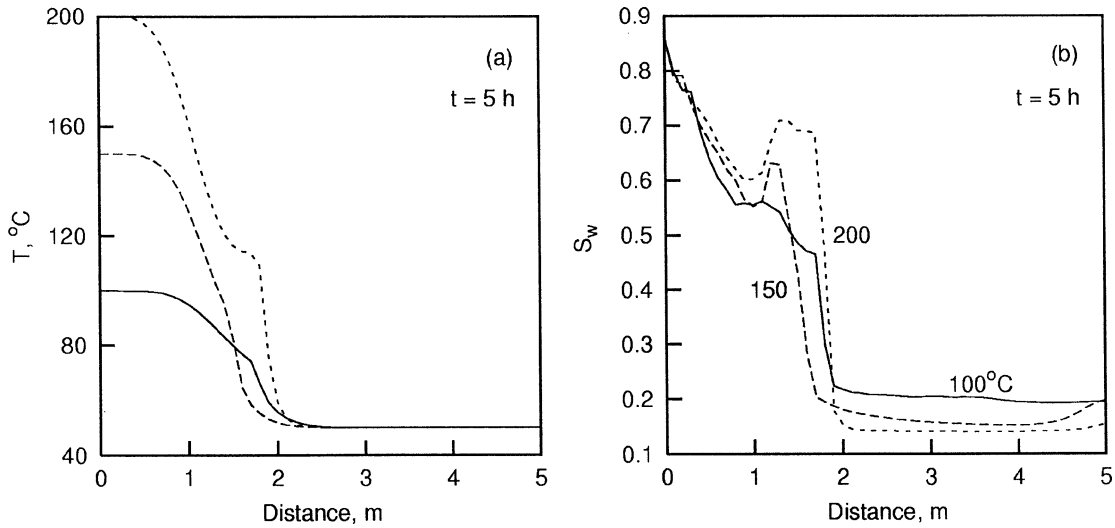

Figure 6. Non-isothermal injection: (a) Temperature profiles in the reservoir as a function of the injection temperature; (b) Effect of the injection temperature on the saturation profile.

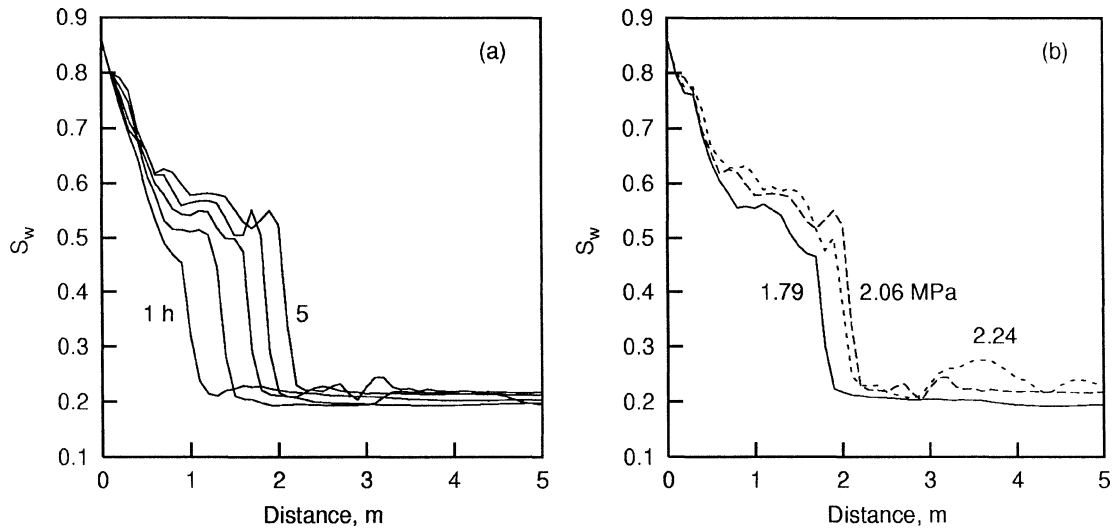

Figure 7. Non-isothermal injection: (a) Evolution of the water saturation front at an injection pressure of 2.06 MPa; (b) Effect of injection pressure on water saturation ($t = 5$ h).

leading to the accumulation of oil and the consequent increase in the overall resistance to flow. At this stage, the composite fluid velocity ahead of the front is also lowered, resulting in a reduced displacement of oil. This is the origin of the local minimum in water saturation in the region closer to the inflow plane. This interpretation is supported by the fact that the saturation front has moved a distance of 1 m in the first hour, while it moves the same distance in the next four hours. With the gradual movement of the fluids in the formation, the minimum in the saturation curve is levelled off owing to the compensation from the injected water on the left inflow plane.

Effect of injection pressure. Results have been presented for three different injection pressures namely 1.79, 2.06 and 2.24 MPa. The formation pressure is 1.31 MPa in the present discussion. The formation temperature is 50 °C, while the injection temperature is 100 °C. The evolution of the saturation front with time is presented in *figure 7(a)*. The saturation profiles at the end of 5 hours of injection have been compared in *figure 7(b)* for the three injection pressures. The principal effect of a greater front displacement at a higher pressure is brought out in *figure 7(b)*. The front-dominated movement of saturation profile, characteristic of non-isothermal injection is seen in *figure 7(a)* at all time levels. Of significance is the absence of the saturation minimum ahead of the front at an injection pressure of 2.06 MPa. This supports the explanation given in the earlier section, that the saturation minima are related to the mismatch between the fluid speed and the thermal front speed. This further suggests that elevated pressures can be employed to stabilize the non-isothermal oil displacement process at higher injection temperatures.

Oil recovery. *Figure 8(a)–(c)* show a comprehensive plot of oil recovery in terms of PPV as a function of time for hot water injection. The individual effects of injection pressure, injection temperature and formation temperature have been respectively shown. The increase in PPV with pressure is gradual and predictable. For the conditions shown in *figure 8(a)*, a pressure of 2.06 MPa leads to a linear increase in PPV with time, a clearly desirable requirement of EOR. It is a consequence of the increased pressure overcoming the problems of oil accumulation and the formation of a saturation minimum, that are unique to non-isothermal injection (*figures 6* and *7*). At a higher pressure of 2.24 MPa, the slope of the PPV curve is higher and further increases with time. The higher slope is related to a greater fluid speed, resulting in a greater portion of the reservoir being cleared of oil. Simultaneously, the overall viscous resis-

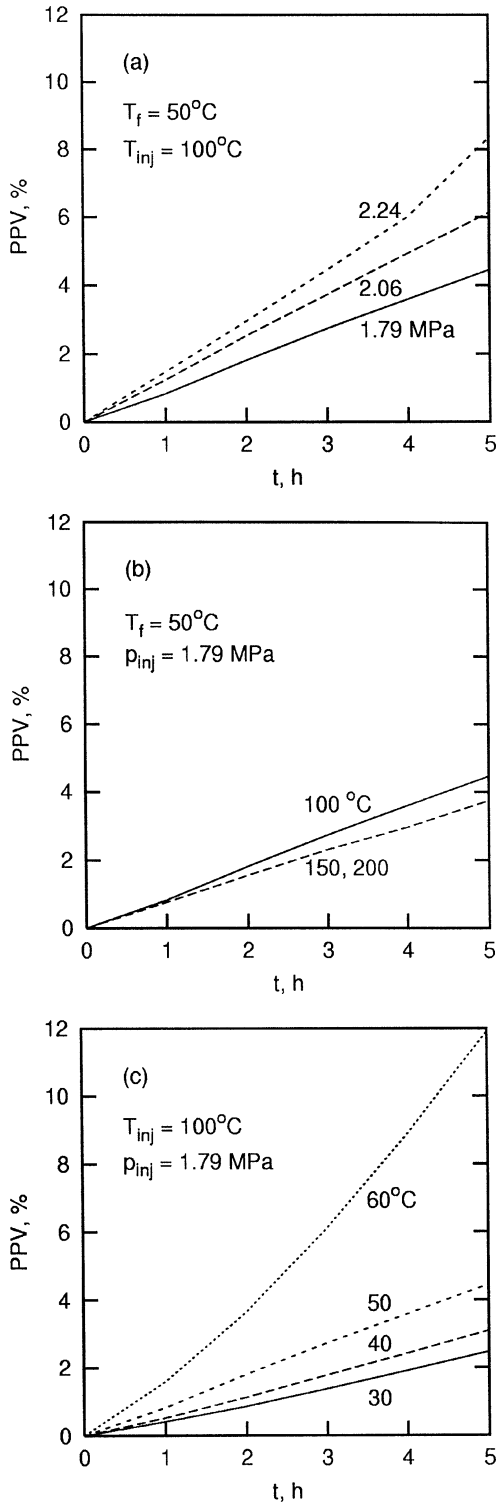

Figure 8. Increase in oil recovery with time during non-isothermal injection: Effect of: (a) Injection pressure; (b) Injection temperature; (c) Formation temperature.

tance falls, leading to a further increase in the fluid speed and a higher rate of oil recovery.

Figure 8(b) shows the influence of injection temperature on PPV. It is to be noted that the PPV values are smaller compared to *figure 8(a)* and the slopes are also smaller. The slopes tend to reduce with time. These trends are in agreement with the observations from *figures 6* and *7*. They point towards the need to optimize the EOR parameters, particularly the injection pressure with respect to the injection temperature.

Figure 8(c) shows the effect of the formation temperature on PPV, for given values of the injection pressure and temperature. An increase in the slope of the PPV curve with the formation temperature is consistently seen. The variation is close to linear for the formation temperatures upto 50 °C. A sharp increase in PPV as well as the slope at a formation temperature of 60 °C owing to a large reduction in the oil viscosity is also revealed in this figure. It is conceivable that even at 60 °C, suitable injection temperature and pressure can be found, that will stabilize displacement of oil by water and result in an improved performance in terms of PPV.

4.2. Treatment of numerical oscillations

For long integration times, oscillations were seen in the numerical solution of the oil recovery equations. The oscillations appeared first in the saturation profiles, leading subsequently to a divergence in the iteration scheme. The nature of these oscillations and the method of treating them are discussed in the present section. The discussion is in terms of the isothermal injection problem with an injection pressure of 1.79 MPa, formation pressure of 1.31 MPa and a formation temperature of 50 °C. Owing to a faster movement of the saturation front, oscillations were not observable during non-isothermal injection, for the range of parameters studied.

Figure 9(a) shows the saturation profile in a 4 m × 0.8 m region after five hours of injection. The solution can be seen to be completely affected by oscillations. The oscillations were seen to appear first after 2 hours. Further, they originated at the outflow plane, indicating their numerical origin associated with the Dirichlet boundary condition at this location. *Figure 9(b)* shows the saturation profile in a larger domain of size 10 m × 1.2 m at the end of 25 hours of injection. The appearance of oscillations owing to the Dirichlet boundary condition at the outflow plane can be seen to be delayed for this longer region. *Figure 9(c)* is a plot of the saturation profile in a 30 m × 1.5 m region at the end of 15 hours of injection. Oscillations induced by reflection at the outflow plane are not visible in this figure. The grid used here is 301 × 11, indicating a significant increase in round-off. The scatter in saturation data for this region in *figure 9(c)* can be traced to this factor. The delay in the appearance of oscillations in longer regions suggests a strategy of controlling them.

The oscillations in the solution can be controlled by periodically smoothing the numerical solution. This can be accomplished by fitting piecewsie splines or polynomials through the water saturation data. This in effect re-initializes the saturation profile for subsequent time-marching. When employed on regions of short lengths, this strategy is expected to delay the appearance of oscillations. Oscillations however will necessarily appear when the saturation front approaches the outflow plane. In physical terms, it can be explained as follows: The movement of the saturation front will tend to increase the saturation level at the outflow plane, violate the Dirichlet boundary condition and the resulting errors will be reflected upstream. The smoothing approach also has the drawback of increasing the CPU time. In the present study, smoothing was applied at intervals of one and two hours. Satisfactory results were obtained in both instances, though two hour intervals required less CPU time. The saturation profiles with this strategy have been shown by dashed lines in *figure 9 (d)* and *(e)* for the 4 m × 0.8 m and 10 m × 1.2 m domains, respectively. In *figure 9(d)*, incipient oscillations are seen after 5 hours of injection. There are oscillations in *figure 9(e)* as well, but these are related to the round-off errors, not the outflow boundary condition. The solution on a 30 m × 1.5 m domain was unaffected by the smoothing of the saturation profile at the end of 15 hours. Irreversible oscillations were initiated in this geometry only after 40 hours of injection.

The third approach adopted for treating the difficulties with the Dirichlet outflow boundary condition is to replace it with a Neumann condition of the type

$$\frac{\partial S_{\mathrm{w}}}{\partial x} = 0$$

This is a non-reflective boundary condition which permits (a) a gradual passage of the oil–water mixture out of the physical domain and (b) a slow build-up of the water saturation at the outflow plane. It is hence expected to reduce oscillations in saturation. Factor (b) is in contrast to the Dirichlet condition, where the saturation is mainatined a constant. The implication is that the solutions obtained with the Dirichlet and Neumann outflow

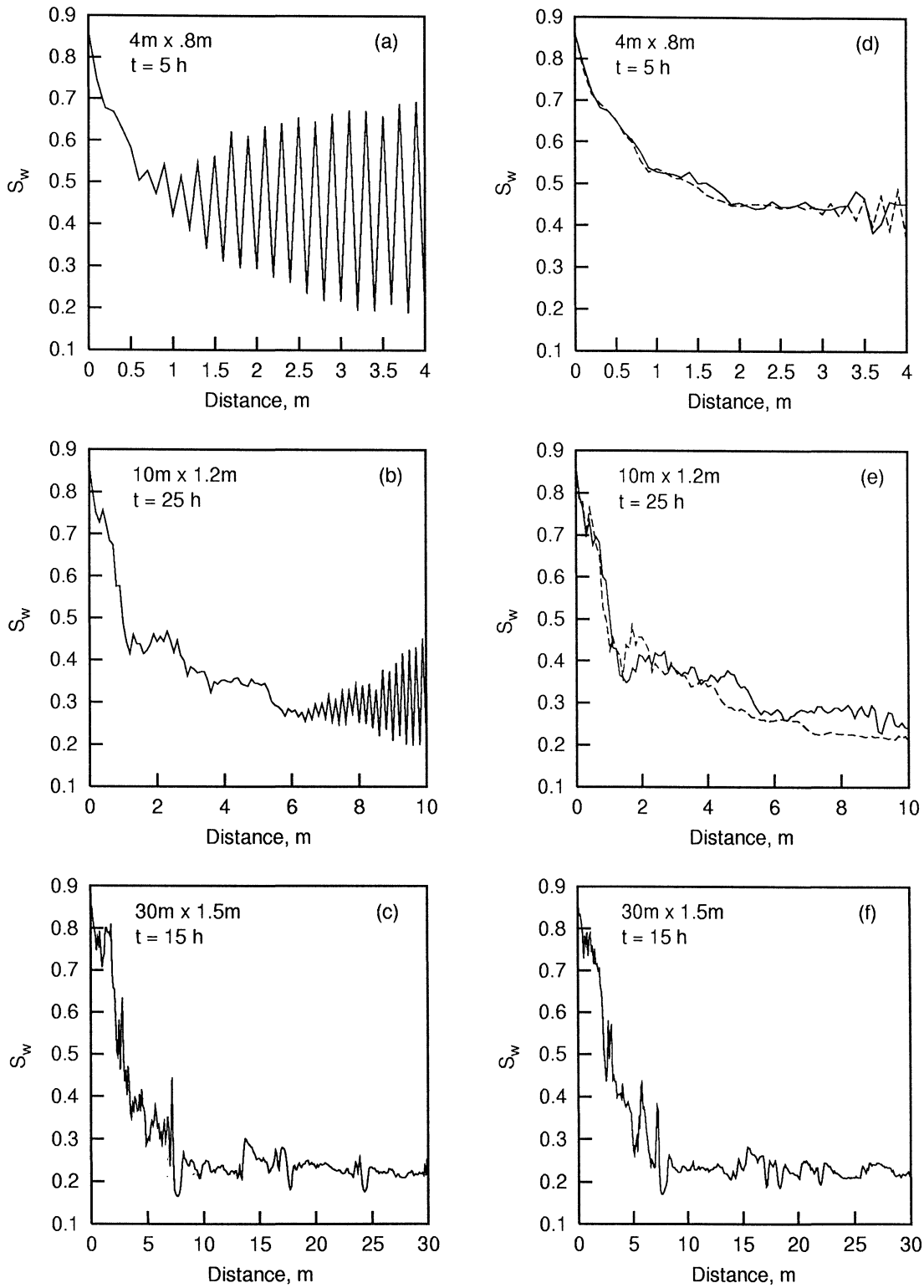

Figure 9. Effect of the outflow boundary condition: (a)–(c) $S_w = 0.2$; (d)–(e) Solid line—periodically smoothed, dashed line—$\partial S_w/\partial x = 0$; (f) Periodically smoothed solution overlaps the solution for Neumann boundary condition.

boundary conditions are different and constitute an uncertainty in the mathematical model itself.

The Neumann boundary condition has been implemented in the form

$$S_{w,M,j} = S_{w,M-1,j}$$

followed by a calculation of the capillary pressure and the oil pressure. In non-isothermal injection, a Neumann boundary condition for temperature must be simultaneously applied. The change of the outflow boundary condition did not lead to any perceptible increase in the CPU time.

The saturation profiles obtained with the Neumann boundary condition are shown by solid lines in *figure 9(d)–(f)*. It can be seen that oscillations are eliminated in the longer domains, though they make an appearance in the 4 m × 0.8 m region at the end of 5 hours (*figure 9(d)*). Besides, the solutions obtained with numerical smoothing and the Neumann boundary condition are qualitatively similar.

The three methods of delaying oscillations discussed above essentially alter the numerical solution itself. Thus they reflect the uncertainty associated with the mathematical model. This uncertainty is best determined in terms of the oil recovery, namely PPV. *Figure 10(a)–(c)* show PPV versus time for the 4 m, 10 m and 30 m domains with the Dirichlet outflow boundary condition, with numerical smoothing and with the Neumann boundary condition. For short time, namely less than two hours, all the three solutions are quite close to one another. The PPV trends start to deviate at longer times. For the 4 m domain, the smoothing and Neumann boundary condition approaches show similar values of PPV. With the Dirichlet boundary condition, the PPV curve levels off after about 10 hours owing to the superimposed oscillations. The other two approaches show a continuous increase in PPV over the entire duration of interest. For 10 m domain, PPV curves over a 25 hour time period for all the three approaches nearly overlap. Differences are however to be seen in the slopes for longer times. The PPV curves are thus expected to diverge after 25 hours, the prediction with the Dirichlet boundary condition being the lowest, and that of the Neumann condition being the highest. The 30 m domain does not experience oscillations due to Dirichlet condition at the outflow boundary but experiences noise over the domain due to round-off as shown in *figure 9(c)*. Therefore the PPV profiles for the first and third approaches are nearly coincident. With numerical smoothing after every two hours, the round-off errors are expected to be within limits. The corresponding plot of PPV is below the others, but in view of the reduction of

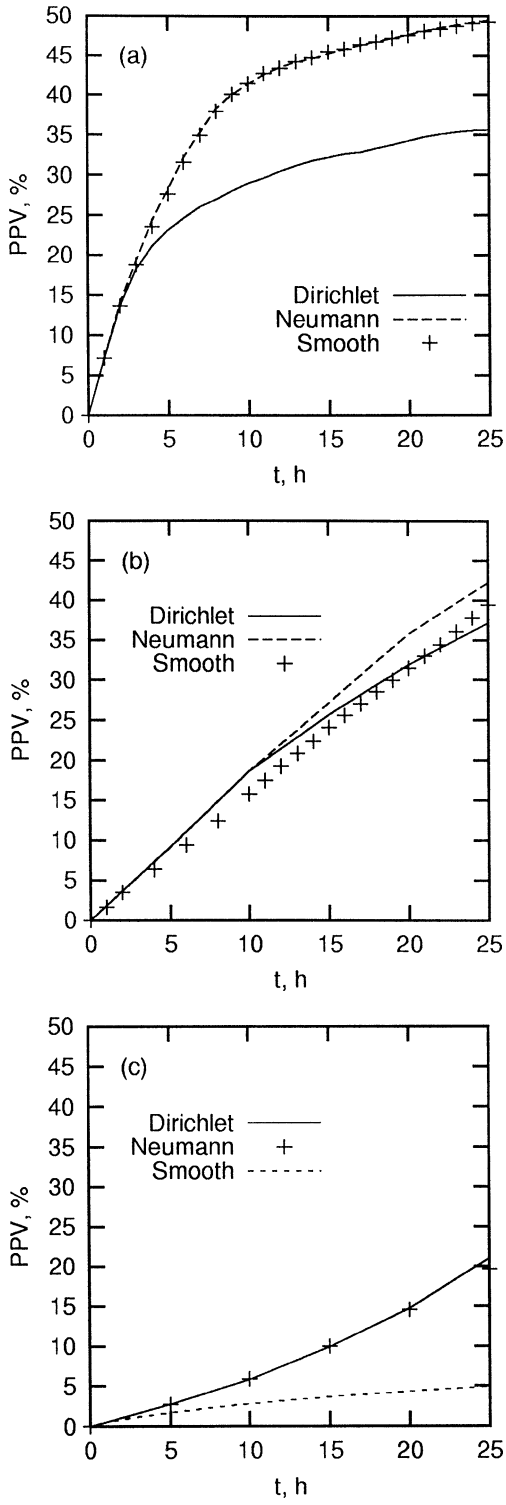

Figure 10. Effect of the Dirichlet outflow boundary condition, Neumann outflow boundary condition and smoothing on oil recovery; Domain size: (a) 4 m; (b) 10 m; and (c) 30 m.

round-off, it may be considered to be the best numerical solution for the 30 m domain.

4.3. Domain decomposition

The suitability of domain decomposition techniques for the simulation of EOR is discussed in the present section. The test case taken up for assessment is isothermal injection in a physical domain of size 10 m $\times$ 1.2 m and a grid size of 101 $\times$ 11. The formation temperature is 50 °C and the injection and formation pressures are 1.79 and 1.31 MPa, respectively. Two domain decomposition algorithms namely Schwarz's [15] and Uzawa's [12] have been considered in the study. The statements of these algorithms have been presented in Section 3.1. The convergence criteria employed are respectively 0.1% in the subdomains and 5E-04 (MPa/m) for the pressure gradient in the interface iterations.

The physical region in the EOR simulation has been divided into 2 and 4 subdomains for analysis. The partitions are vertical. A comparison of the solutions in terms of water saturation for two and four subdomains with Schwarz's algorithm is shown in *figure 11 (a)* and *(b)*. The two solutions are close to each other and also to the single domain profile, particularly for early time, showing that the domain decomposition algorithms have converged to practically the same solution. Similar results have been obtained with the Uzawa's algorithm. On the other hand, all the solutions are affected by the outflow plane oscillations. The solutions with domain decomposition are affected to a greater extent in terms of the error amplitude near the outflow plane. The oscillations are seen to fill the second domain in *figure 11(a)*. To examine this aspect further, numerical calculations have been carried out on four subdomains with the Schwarz's algorithm (*figure 11(b)*). The oscillations are seen to be considerably reduced in the bulk of the formation, but fills entirely the fourth subdomain. Thus domain decomposition also emerges as a strategy for controlling oscillations induced by restrictive outflow boundary conditions.

It is to be noted that the domain decomposition algorithms responded well to both oscillation control strategies, namely the outflow plane Neumann condition and periodic smoothing.

In the context of domain decomposition, the principal issues that require analysis are (1). the changes in the CPU time with increasing number of subdomains, and (2). optimization with respect to the interface relaxation factor. This discussion is presented below.

The CPU times recorded with a relaxation factor of $\theta = 0.25$ on various grids with the Schwarz's technique is presented in *table I*. The computed PPV in each case as well as the value obtained from a full domain have been included for comparison. The comparison is seen to be satisfactory. The CPU times for a 101 $\times$ 11 grid with different values of θ are presented in *table II*. A value of $\theta = 0.1$ emerges as an optimum in the present study. The CPU times for 2 and 4 subdomains are significantly higher than that for a single domain.

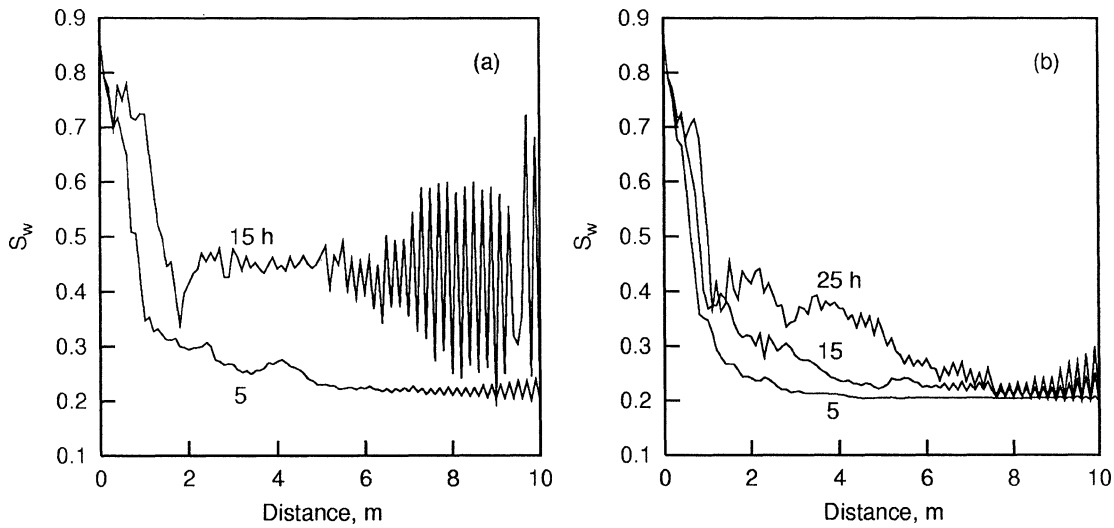

Figure 11. Control of oscillations in: (a) two; and (b) four subdomain models using Schwarz's algorithm. Region size 10×1.2 m, Grid 101×11.

TABLE I
Performance of the Schwarz technique on various grids and domain sizes.

Domains			1		2	
Grid	Domain, m	Time, h	PPV	CPU (h:m:s)	PPV	CPU (h:m:s)
101 × 11	10 × 1.2	5	5.81	0:6:37	5.8	0:29:54
101 × 11	10 × 1.2	10	14.2	0:12:44	14.1	1:07:33
301 × 11	30 × 1.5	5	1.63	0:59:35	1.47	3:05:05
301 × 11	30 × 1.5	10	3.57	3:03:28	3.4	9:23:48

TABLE II
Performance of the Schwarz technique with respect to the interface parameter in terms of CPU time (h:m:s); Grid 101 × 11; Domain 10 m × 1.2 m.

Subdomains	Time, h	$\theta = 0.05$	0.1	0.25
2	5	24:21	26:02	29:54
2	10	55:02	57:45	1:04:09
4	5	25:23	24:25	29:52
4	10	53:51	52:31	1:04:19

A possible explanation is that in the subdomain, the matrix size is smaller but the bandwidth of the matrix is unchanged. Thus the sparsity pattern of the matrix is actually increased. The approximate L–U factorization is less satisfactory in this context and results in an increased CPU time. In summary, the advantages of a reduced memory requirement and better control of oscillations, is counter-balanced by an increase of more than N-fold in the CPU time, where N is the number of subdomains.

With Uzawa's algorithm, an unexpected difficulty was encountered. Convergence was obtained only when the domain was divided into two subdomains. Even here, the CPU time was found to be quite large. For a larger number of subdomains, the top and bottom boundaries being impermeable, the intermediate subdomains had all Neumann boundary conditions. In view of the slow transients in the porous formation, it led to the possibility of non-uniqueness in the solution for these subdomains. Consequently, convergence could not be obtained. The CPU times for two subdomains with varying values of the interface parameter α are given in *table III*. A value of $\alpha = 0.1$ can be seen to be an optimum for the present simulation.

Both Schwarz's and Uzawa's algorithms were however successfully applied to two and four subdomains when the interfaces were taken to be horizontal. The subdomains prevailed over the entire length of the porous layer. The appearance of a pure Neumann problem was avoided here and there was no difficulty with convergence. There was an additional benefit of a reduced bandwidth of the matrix to be inverted, since node-numbering was carried out in the direction transverse to the porous layer. Special treatment for numerical oscillations was however required in the calculations. The CPU times for the simulation with Uzawa's algorithm are presented in *table IV*. It can be seen here that the increase in CPU time over a full domain calculation is negligible. This points towards the possibility of successfully parallelizing the domain decomposition algorithms.

TABLE III
Performance of Uzawa's algorithm with respect to the interface parameter in terms of the CPU time (h:m:s); Grid 101 × 11; Domain 10 m × 1.2 m; Two subdomains; Vertical domain partitioning.

Time, h	$\alpha = 0.05$	0.1	0.15
5	52:39	29:10	33:56
7	1:39:01	47:20	48:34

TABLE IV
Performance of Uzawa's algorithm with respect to the interface parameter in terms of the CPU time (m:s); Grid 101 × 11; Domain 10 m × 1.2 m; Horizontal domain partitioning.

Subdomains	Time, h		$\alpha = 0.05$	0.1	0.15
1	5	6:37			
1	10	12:44			
2	5		7:09	7:09	7:10
2	10		16:17	16:15	16:13
4	5		6.51	6:51	6:52
4	10		14:46	14:52	14:59

CONCLUSIONS

Numerical simulation of oil recovery from a porous formation has been reported in the present work. Along with the parametric study of the baseline reservoir performance, the growth and control of discretization errors

and the utility of domain decomposition techniques have been discussed. The following conclusions have been arrived at in the present study:

(1) In isothermal injection, the water saturation profiles are diffusion-dominated. With increasing formation temperature, the viscous resistance reduces over the entire domain. Hence, there is significant increase in oil recovery. There is also an increase in oil recovery with the increase in the injection pressure.

(2) At longer times, the use of a Dirichlet boundary condition on the outflow plane is a source of numerical oscillations. Numerical smoothing and a Neumann boundary condition delay the appearance of oscillations.

(3) During non-isothermal injection, the saturation profiles are front-dominated and correlate well with the temperature profiles. Oil is mobilized rapidly, leading to the formation of an oil pool ahead of the water front. This results in a non-uniform rate of oil recovery. The adverse effect of non-isothermal injection is counter-balanced by an increase in the injection pressure. Numerical oscillations have not been observed here for the duration of injection studied.

(4) Domain decomposition using Schwarz's and Uzawa's algorithms for interface treatment have been implemented in the present work. Vertical subdivision of the physical region was seen to isolate the numerical oscillations to the last subdomain alone. There was however a penalty of an increased CPU time. A distinct CPU time advantage was seen in adopting a horizontal partitioning of the physical region instead of the vertical. This was because it avoided the pure Neumann problem over the subdomains and reduced the bandwidth of the matrix to be inverted.

REFERENCES

[1] Lake L.W., Enhanced Oil Recovery, Prentice-Hall, New Jersy, 1989.

[2] Aziz K., Modeling of thermal oil recovery processes, in: Fitzgibbon W.E. (Ed.), Mathematical and Computational Methods in Siesmic Exploration and Reservoir Modeling, SIAM, Philadelphia, PA, 1986, pp. 3–17.

[3] Wang C.Y., Modeling multiphase flow and transport in porous media, in: Ingham D.B., Pop I. (Eds.), Transport Phenomena in Porous Media, Pergamon, London, 1998, pp. 383–410.

[4] Ewing R.E., The Mathematics of Reservoir Simulation, SIAM, Philadelphia, PA, 1983.

[5] Stevenson M.D., Kagan M., Pinczewski W.V., Computational methods in petroleum reservoir simulation, Comput. Fluids 19 (1991) 1–19.

[6] Douglas J., Finite difference methods for two-phase incompressible flow in porous media, SIAM J. Numer. Anal. 20 (1983) 681–696.

[7] Boberg T.C., Thermal Methods of Oil Recovery: An Exxon Monograph, Wiley, New York, 1988.

[8] Vinsome P.K.W., Fully implicit versus dynamic implicit reservoir simulation, J. Canad. Petro. Tech. (1985) 49–82.

[9] Pillai K.M., Muralidhar K., A numerical study of oil recovery using water injection method, Numer. Heat Transfer 24 (1993) 305–322.

[10] Duff I.S., MA28-A set of fortran subroutines for sparse unsymmetric linear equations, AERE Harwell, 1980.

[11] Tallec P.Le, Domain decomposition methods in computational mechanics, Comput. Mechanics Adv. 1 (2) (1994) 121–220.

[12] Yagawa G., Soneda N., Yoshimura S., A large scale finite element analysis using domain decomposition method on a parallel computer, Comput. Structures 38 (5/6) (1991) 615–625.

[13] Chan T.F., Smith B.F., Domain decomposition and multigrid algorithm for elliptic problems on unstructured meshes, Contemp. Math. 180 (1994) 175–189.

[14] Smith B.F., Bjorstad P., Gropp W., Domain Decomposition: Parallel Multilevel Methods for Elliptic Partial Differential Equations, Cambridge Univ. Press, Cambridge, 1997.

[15] Funero D., Quarteroni A., Zanolli P., An iterative procedure with interface relaxation for domain decomposition methods, SIAM J. Numer. Anal. 25 (6) (1988) 1213–1236.

APPENDIX A: MATERIAL PROPERTIES

The properties required to close the system of equations (3)–(5) are specified below.

TABLE A.I
Oil viscosity as a function of temperature.

T, °F	50	150	250	350	450
μ_o, cP	5000	126	20	7.1	4.0

TABLE A.II
Constitutive relations for the porous formation (from [7]).

S_w	k_{rw}	k_{ro}	$p_{c_{ow}}$ (psi)
0.1	0.0	1.0	4.111
0.2	0.0016	0.875	0.095
0.3	0.0081	0.735	0.072
0.4	0.0259	0.590	0.061
0.5	0.0672	0.420	0.051
0.6	0.1000	0.210	0.041
0.7	0.1400	0.070	0.031
0.8	0.2000	0.016	0.021
0.86	0.2500	0.0	0.011

TABLE III
Fluid and formation properties.

K	k_h	ε	ξ_o	ξ_w	β_o	β_w	c_o	c_w	$(\rho c)_R$	ρ_o	ρ_w
(Darcies)	($W \cdot m^{-1}$ °C)		(Pa^{-1})		(°C^{-1})		($J \cdot kg^{-1}$ °C)		kJ·m^{-3} °C	($kg \cdot m^{-3}$)	
132	0.1661	0.375	0.03447	0.02137	2.28	2.28	2092	4184	2413	900	1000

TABLE IV
Water viscosity as a function of temperature.

T, °F	60	75	80	100	120	150	200	250	300	400	500
μ_w, cP	1.130	0.935	0.875	0.685	0.560	0.430	0.308	0.230	0.182	0.145	0.120